JACS
JOURNAL OF THE AMERICAN CHEMICAL SOCIETY

Article

pubs.acs.org/JACS

Confinement of Ultrasmall Cu/ZnO_x Nanoparticles in Metal–Organic Frameworks for Selective Methanol Synthesis from Catalytic Hydrogenation of CO_2

Bing An,[†] Jingzheng Zhang,[†] Kang Cheng,[†] Pengfei Ji,[‡] Cheng Wang,*[,†] and Wenbin Lin*[,†,‡]

[†]Collaborative Innovation Center of Chemistry for Energy Materials, State Key Laboratory of Physical Chemistry of Solid Surfaces, Department of Chemistry, College of Chemistry and Chemical Engineering, Xiamen University, Xiamen 361005, PR China

[‡]Department of Chemistry, University of Chicago, 929 East 57th Street, Chicago, Illinois 60637, United States

Supporting Information

ABSTRACT: The interfaces of Cu/ZnO and Cu/ZrO_2 play vital roles in the hydrogenation of CO_2 to methanol by these composite catalysts. Surface structural reorganization and particle growth during catalysis deleteriously reduce these active interfaces, diminishing both catalytic activities and MeOH selectivities. Here we report the use of preassembled bpy and $Zr_6(\mu_3\text{-}O)_4(\mu_3\text{-}OH)_4$ sites in UiO-bpy metal–organic frameworks (MOFs) to anchor ultrasmall Cu/ZnO_x nanoparticles, thus preventing the agglomeration of Cu NPs and phase separation between Cu and ZnO_x in MOF-cavity-confined Cu/ZnO_x nanoparticles. The resultant Cu/ZnO_x@MOF catalysts show very high activity with a space–time yield of up to 2.59 g_{MeOH} kg_{Cu}^{-1} h^{-1}, 100% selectivity for CO_2 hydrogenation to methanol, and high stability over 100 h. These new types of strong metal–support interactions between metallic nanoparticles and organic chelates/metal-oxo clusters offer new opportunities in fine-tuning catalytic activities and selectivities of metal nanoparticles@MOFs.

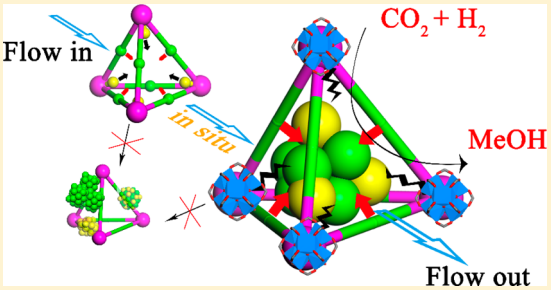

INTRODUCTION

As methanol is a potential clean fuel as well as an important feedstock to produce commodity chemicals,[1] the catalytic conversion of CO_2 to methanol is a highly desirable chemical process that can also combat the rising CO_2 level in Earth's atmosphere.[2] The ternary Cu/ZnO/Al_2O_3 catalyst is industrially used in methanol systhesis from syngas (CO/H_2) and also from CO_2 hydrogenation.[3] In the latter, CO_2 is the direct carbon source for the methanol production as revealed by isotopic labeling studies.[4] Although the detailed structure of the active catalytic site is still under debate, there is a consensus on the critial role of the Cu/ZnO_x interface.[5] However, Cu nanoparticles (NPs) slowly aggregate and separate from ZnO_x under reaction conditions, reducing the Cu/ZnO_x interfaces and diminishing the catalytic activity over time.[6] Because the Cu surface can catalyze the reversed water–gas shift (RWGS) reaction to convert CO_2 to CO, phase-separated catalysts exhibit poor selectivity for methanol.[3b,7] Stabilizing intimately mixed Cu/ZnO_x interfaces is thus crucial to maintaining high catalytic activity and selectivity.

Strong metal–support interactions (SMSIs) and confinement effects have previously been used to stabilize Cu NPs in catalytic CO_2 hydrogenation.[8] For example, zirconia as a carrier interacts more strongly with Cu as compared to alumina, leading to more dispersed NPs and enhanced catalyst stability.[9] Mesoporous zeolites were also used to prevent NP growth by confining them in the nanochannels.[8d,10] We envision that porous metal–organic frameworks (MOFs) can combine both the confinement effect by the pores and the SMSIs with orthogonal metal-coordinating sites from the ligands and metal-oxo cluster secondary building units (SBUs) to provide a novel carrier for Cu-based CO_2 hydrogenation catalysts.

MOFs possess regular pores and cavities for NP encapsulation and have served as functionalized supports for highly active catalysts.[11] For example, Yaghi and Somorjai recently reported core–shell structures composed of 18 nm Cu NPs in the cores and porous MOFs in the shells for CO_2 hydrogenation with high selectivity.[8a] Organic coordinating groups on the MOF struts can further stabilize NPs and tune their surface structures by specific SMSIs.[12] Alternatively, the SBUs in Zr-based MOFs were recently explored as novel supports for single-site catalysts.[13] We hypothesized that these SBU sites could also act as oxometalate anchors for metal/metal oxide NPs. The combination of cavity confinement effects with specific and tunable SMSIs provides a unique opportunity to stabilize well-mixed ultrasmall Cu/ZnO_x NPs for CO_2 hydrogenation.

In this work, we used UiO-bpy MOF, constructed from linear 2,2′-bipyridine-5,5′-dicarboxylate (bpydc) bridging ligands and $Zr_6(\mu_3\text{-}O)_4(\mu_3\text{-}OH)_4$ SBUs, as a support for Cu/ZnO_x catalysts (Scheme 1). UiO-bpy possesses exceptional

Received: January 3, 2017
Published: February 17, 2017

DOI: 10.1021/jacs.7b00058
J. Am. Chem. Soc. 2017, 139, 3834–3840

Scheme 1. Preparation of CuZn@UiO-bpy via *in Situ* Reduction of Post-Synthetically Metalated UiO-bpy[a]

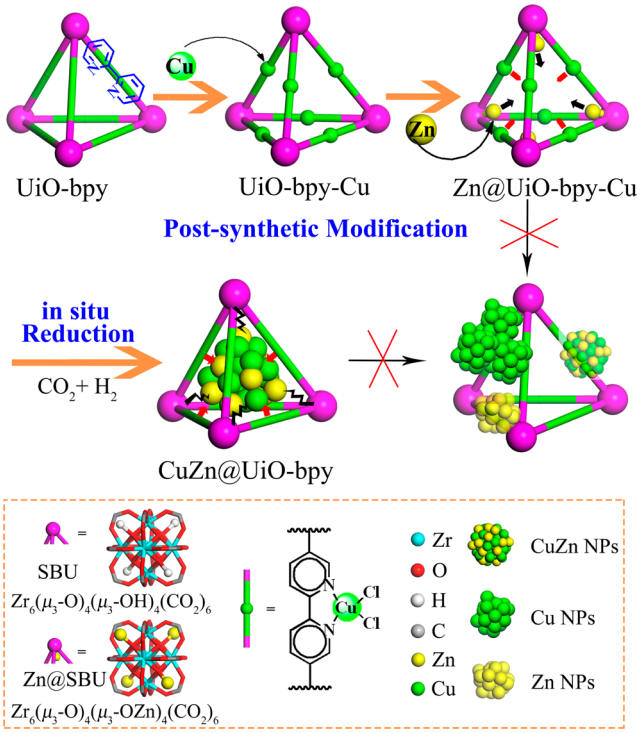

[a]Cu^{2+} ions were coordinated to the bpy groups, while Zn^{2+} ions were attached to the SBUs.

thermal stability (>250 °C) even under high humidity.[14] Cu^{2+} ions were first coordinated to the bpy sites in the MOF by postsynthetic metalation with $CuCl_2$. Zn^{2+} ions were then introduced by reacting $ZnEt_2$ with the μ_3-OH sites on the SBUs. Ultrasmall Cu/ZnO_x NPs were generated *in situ* at a reaction temperature of 250 °C in the presence of H_2 as the reductant. These NPs of smaller than 1 nm diameter reside in the tetrahedral and octahedral cages confined by the ligands to afford novel Cu/ZnO_x@MOF catalysts with high activity and selectivity for CO_2 hydrogenation to methanol.

RESULTS

Synthesis and Characterization of the CuZn@UiO-bpy Catalyst with MOF-Cavity-Confined Ultrasmall Cu/ZnO_x Nanoparticles. UiO-bpy was synthesized via a solvothermal reaction between $ZrCl_4$ and H_2bpydc in the presence of HCO_2H (Supporting Information Section 3). UiO-bpy is isostructural to UiO-67, which is constructed from 12-connected $[Zr_6(\mu_3\text{-}O)_4(\mu_3\text{-}OH)_4]^{12+}$ SBUs and linear dicarboxylate ligands in a fcu topology. UiO-bpy contained 9.1% of formates (based on total carboxylates) on the SBUs as determined by ^{1}H NMR spectra of the digested MOFs (Figure S1). Thermogravimetric analysis (TGA) gave 37.7% weight loss in the temperature range of 400−500 °C (Figure S2) due to ligand decomposition, suggesting a bpydc/Zr molar ratio of $^5/_6$ that is consistent with coordiantion defects on the SBUs. UiO-bpy thus has many coordination defects and possesses an approximate formula of $Zr_6(\mu_3\text{-}O)_4(\mu_3\text{-}OH)_4(\mu_1\text{-}OH)(H_2O)\text{-}(bpydc)_5(HCO_2)$ (Supporting Information Section 3). The coordinated formate groups decompose under reaction conditions, as clearly evidenced by the disappearance of the ν(C−H) stretching peak of formate at 2873 and 2966 cm^{-1} in the *in situ* diffuse-reflectance infrared Fourier transform (DRIFT) spectra at 150 °C (Figure S3). The open coordination sites on the SBUs can adsorb and activate CO_2 under catalytic conditions.

UiO-bpy was treated with $CuCl_2$ in THF to afford UiO-bpy-Cu (Figures 1 and S4). The coordination of Cu ions to bpydc

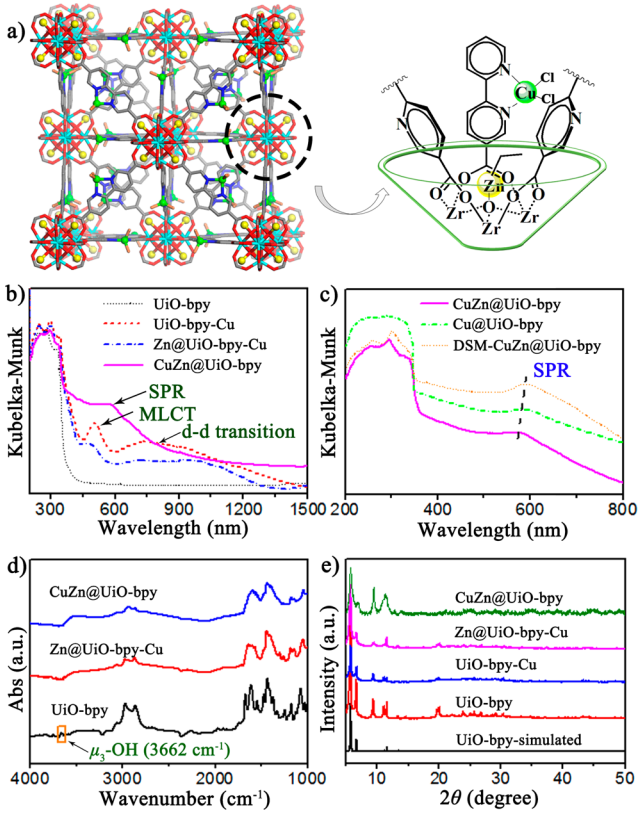

Figure 1. Structures and characterization of Cu- and Zn-functionalized UiO-bpy. (a) Idealized structure of the precatalyst, Zn@UiO-bpy-Cu, via postsynthetic Cu coordination to bpy followed by protonolysis of $Zr_3(\mu_3\text{-}OH)$ sites on UiO-bpy-Cu SBUs with $ZnEt_2$. Diffuse reflectance UV−vis−NIR spectra (b), shift of SPR peaks (c), IR spectra (d), and powder X-ray diffraction patterns (e) of UiO-bpy and its postsynthetically metalated derivatives.

was supported by the presence of a metal-to-ligand charge transfer (MLCT) band at 470−530 nm and a Cu^{2+} d−d transition at ∼720 nm in the diffuse reflectance UV−vis−NIR spectra of UiO-bpy-Cu (Figure 1b).[15] The $Zr_3(\mu_3\text{-}OH)$ sites on UiO-bpy-Cu SBUs were metalated with $ZnEt_2$ to afford $Zr_3(\mu_4\text{-}OZnEt)$ in Zn@UiO-bpy-Cu. The coordination of Zn ions in Zn@UiO-bpy-Cu was confirmed by the disappearance of the $\nu(\mu_3\text{-}OH)$ vibrational band at 3662 cm^{-1} in the infrared spectra after metalation with $ZnEt_2$ (Figure 1d). Every μ_4-O-ZnEt moiety is in close proximity to six carboxylate oxygen atoms from the ligands that create a unique bowl-shaped coordination environment for Zn ions.

Powder X-ray diffraction (PXRD) studies demonstrated that all metalated UiO-bpy materials remained crystalline (Figure 1e). The Cu loading as determined by inductively coupled plasma-optical emission spectrometry (ICP-OES) corresponded to the coordination of 77% of the bpy sites in UiO-bpy whereas Zn occupied 100% of the $Zr_3(\mu_3\text{-}OH)$ sites. An approximate chemical formula of Zn@UiO-bpy-Cu was thus

DOI: 10.1021/jacs.7b00058
J. Am. Chem. Soc. 2017, 139, 3834−3840

determined to be $Zr_6(\mu_3\text{-}O)_4(\mu_3\text{-}OZnEt)_4(\mu_1\text{-}OH)(H_2O)\text{-}(bpydc)_{1.15}(bpydc\text{-}CuCl_2)_{3.85}(HCO_2)$.

Nitrogen sorption experiments gave BET surface areas of 324.3 m^2/g for UiO-bpy-Cu and 89.8 m^2/g for Zn@UiO-bpy-Cu, which are both much smaller than that of the unmetalated MOFs (3037 m^2/g) (Figure S5). The reduction of BET surface area after metalation is consistent with high metal loadings and the potential blocking of pore entrances by the sterically demanding $-CuCl_2$ and $-ZnEt$ moieties.

Zn@UiO-bpy-Cu was *in situ* reduced to form the CuZn@UiO-bpy catalyst at 250 °C and 4 MPa with a H_2/CO_2 ratio of 3. The redution of Cu species was supported by temperature-programmed reduction (TPR) with hydrogen (H_2-TPR) (Figure S6), which exhibited a broad peak in the temperature range of 130−250 °C that is consistent with the reduction of Cu(II) to Cu(0) in the presence of SMSIs.[16] X-ray photoelectron spectroscopy (XPS) demonstrated that CuZn@UiO-bpy contained entirely Cu(0) and a mixture of Zn(II) and Zn(0) (see below). As a result, we formulated the active catalyst as ultrasmall Cu/ZnO_x NPs encapsulated in the cavities of UiO-bpy.

Diffuse reflectance UV−vis−NIR spectroscopy revealed the formation of Cu NPs after *in situ* reduction, based on the disappearance of the MLCT and d−d transition bands of the bpy-Cu^{2+} complex and appearance of surface plasmon resonance (SPR) band of Cu NPs at 573 nm (Figure 1b). The position of this SPR peak is consistent with a particle size of less than 1 nm (<30 Cu atoms).[17] These NPs can be confined in the octahedral and tetrahedral cavities inside the MOFs, which are 1.6 and 0.75 nm in diameter, respectively. The formation of ultrasmall Cu NPs is also supported by the high Cu dispersivity of 55.3%, which is defined as the percentage of Cu on the NP surface and measured by N_2O oxidation followed with H_2 titration. Cu/ZnO_x NPs inside UiO-bpy cannot be identified in TEM images (Figures 2 and S7) or PXRD patterns of CuZn@UiO-bpy (Figure 1e), likely due to their small sizes and lack of contrast over Zr_6 SBUs. Energy dispersive X-ray spectroscopy (EDX) mapping indicated uniform distribution of Cu and Zn throughout the particles of both Zn@UiO-bpy-Cu (Figure 2d) and CuZn@UiO-bpy (Figures 2e, S8 and S9; Table S1). The Cu and Zn distributions overlapped with each other, suggesting that Zn and Cu are well-mixed with no phase separation on the length scale less than 10 nm, which is the spatial resolution of EDX.

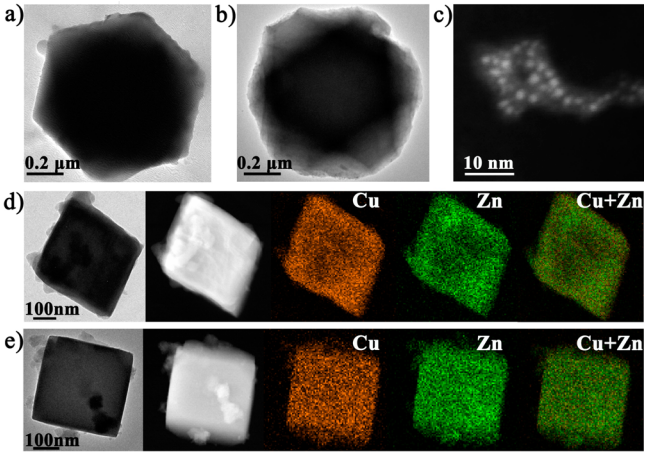

Figure 2. TEM images, HAADF images, and EDX mapping of Zn@UiO-bpy-Cu (a, d) and CuZn@UiO-bpy (b, e). Cu distribution is shown in orange, whereas Zn distribution is shown in green. TEM-EDX mapping studies indicated that Cu and Zn were well-dispersed and mixed throughout the MOF particle. (c) HAADF image of ultrasmall Cu/ZnO_x NPs obtained from digesting CuZn@UiO-bpy with a K_3PO_4 solution in the presence of PVP to stabilize the NPs.

To release the Cu/ZnO_x NPs from CuZn@UiO-bpy for direct TEM characterization, we digested the UiO-framework with a K_3PO_4 solution in the presence of polyvinylpyrrolidone (PVP) to stabilize the ultrasmall NPs and removed zirconium phosphate solid by centrifugation at low speed (7500 rpm, 6500 g). Scanning transmission electron microscopy-high angle annular dark-field (STEM-HAADF) images of the species in the supernatant clearly showed nanoparticles of 0.5−2.0 nm in size (Figures 2c and S10). These ultrasmall NPs contained both Cu and Zn elements as demonstrated by EDX (Figure S11).

Catalytic CO_2 Hydrogenation to Methanol. *Catalytic Performace of CuZn@UiO-bpy.* CuZn@UiO-bpy was tested for CO_2 hydrogenation at 250 °C and 4 MPa with a H_2/CO_2 ratio of 3. CuZn@UiO-bpy exhibited a space−time yield to MeOH (STY_{MeOH}) of 2.59 $g_{MeOH}\ kg_{Cu}^{-1}\ h^{-1}$ at a gas hourly space velocity (GHSV) of 18000 h^{-1}, greatly exceeding the STY_{MeOH} value of 0.83 $g_{MeOH}\ kg_{Cu}^{-1}\ h^{-1}$ for the commercial ternary $Cu/ZnO/Al_2O_3$ catalyst in a 6/3/1 ratio under identical conditions (Tables 1 and S2). More strikingly, CuZn@UiO-bpy gave a 100% selectivity for methanol at 200−250 °C with a GHSV of 18 000 h^{-1}, whereas the ternary $Cu/ZnO/Al_2O_3$ catalyst gave a selectivity of only 54.8% for methanol at 250 °C, owing to the dominance of the RWGS reaction catalyzed by phase-separated Cu NPs. Knowing that low CO_2 conversions (<3%) usually give high methanol selectivity,[18] we also evaluated the catalytic performance at decreased GHSV values and higher CO_2 conversions. At a GHSV of 1600 h^{-1}, we obtained a CO_2 conversion of 17.4% and a high MeOH selectivity of 85.6% for CuZn@UiO-bpy (Figure S12).

The PXRD pattern of the catalyst after reaction was the same as that before the reaction, confirming the preservation of the MOF structure during catalysis (Figure 1e). Consistent with this, TEM and SEM images of the samples after the reaction retained the original shape of MOF particles, and EDX mapping showed even distribution of Cu and Zn throughout the MOF particles (Figure 2b,e).

The catalytic stability of CuZn@UiO-bpy was tested by running the CO_2 hydrogenation reaction for 100 h. The selectivity remained unchanged at 100% for methanol throughout the experiment, and the activity only slightly decreased by less than 10% during 100 h on stream (Figure 3). In comparison, the commercial $Cu/ZnO/Al_2O_3$ catalyst lost half of its activity in the first 15 h. The selectivity for methanol dropped from 62.7 to 44.3% while the CO selectivity increased from 37.3 to 55.7% at the same time.

Influence of Zinc Species on Catalytic Activity. The critical role of Zn in catalysis was revealed by the much lower activity of Cu@UiO-bpy, a sample modified with Cu but not with Zn (Figures S13−15). Cu@UiO-bpy exhibited a STY_{MeOH} of 0.13 $g_{MeOH}\ kg_{Cu}^{-1}\ h^{-1}$ with a low methanol selectivity of 51.9% (for a 30 h run with GHSV of 1600 h^{-1}). Additionally, both STY_{MeOH} and methanol selectivity quickly dropped over 30 h, from 0.30 to 0.13 $g_{MeOH}\ kg_{Cu}^{-1}\ h^{-1}$ and from 73.3 to 51.9%, respectively (Table 1; Figure S16). The diffuse reflectance spectra of Cu@UiO-bpy showed an SPR peak around 582 nm, suggesting the formation of Cu NPs in Cu@UiO-bpy (Figure 1c).[19]

DOI: 10.1021/jacs.7b00058
J. Am. Chem. Soc. 2017, 139, 3834−3840

Table 1. Catalytic Performances of CuZn@UiO-bpy and Control Catalysts in CO_2 Hydrogenation[a]

catalysts	Cu wt %	GHSV (h^{-1})[b]	CO_2 conv. (%)	select. (%) MeOH	select. (%) CO	STY (g_{MeOH} kg_{Cu}^{-1} h^{-1})
		18000	3.3	100	0	2.59
CuZn@UiO-bpy	6.9	6000	7.2	100	0	1.97
		1600	17.4	85.6	14.4	1.12
$Cu/ZnO/Al_2O_3$	38.8	18000	11.1	54.8	45.2	0.83
Cu@UiO-bpy[c]	11.0	1600	5.6	51.9	48.1	0.13
DSM-CuZn@UiO-bpy[d]	5.8	1600	7.1	94.6	5.4	0.58
DSM-CuZn@UiO-67[d]	7.2	1600	8.9	70.8	29.2	0.40
CuZn@MOF-253(Al)	14.9	1600	8.7	93.2	6.8	0.27

[a]Reaction conditions: H_2/CO_2 = 3, P = 4 MPa, time =30 h, F = 30 mL/min, temp. = 250 °C. [b]GHSV = 18 000 h^{-1}, m = 0.1 g; GHSV = 6000 h^{-1}, m = 0.3 g; GHSV = 1600 h^{-1}, m = 0.3 g, F = 8 mL/min. [c]Cu@UiO-bpy was obtained by treating UiO-bpy-Cu with $NaBEt_3H$ before *in situ* reduction. [d]The samples were synthesized via a double solvent method (DSM) with $NaBEt_3H$ as reductant.

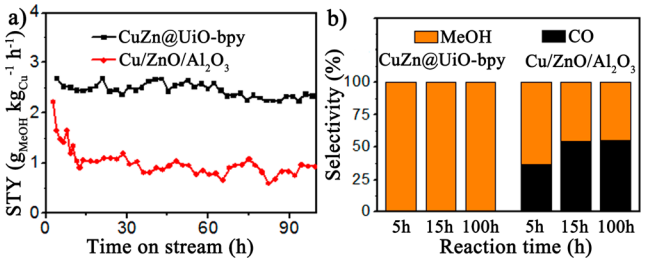

Figure 3. (a) STY of MeOH vs reaction time over a period of 100 h on stream. (b) Selectivity of product vs reaction time.

We also prepared CuZn@UiO-bpy catalysts with different Zn/Cu ratios of 0.26, 0.54, 0.85, and 0.91. As the Zn loading increased, the STY_{MeOH} increased from 1.05 g_{MeOH} kg_{Cu}^{-1} h^{-1} for the catalyst with Zn/Cu = 0.26 to 2.61 g_{MeOH} kg_{Cu}^{-1} h^{-1} for the catalyst with Zn/Cu = 0.91 at a GHSV of 18 000 h^{-1}. Methanol selectivies were 100% for all of these catalysts (Table S3). These results confirm the critical role of ZnO_x in CO_2 hydrogenation.

In Situ versus ex Situ Generated Cu/ZnO$_x$ NPs. We also prepared a control catalyst with *ex situ* generated Cu/ZnO_x NPs (DSM-CuZn@UiO-bpy) by a double-solvent method. Concentrated aqueous solutions of $ZnCl_2$ and $CuCl_2$ were added dropwise to a suspension of UiO-bpy in hexane under vigorous stirring.[20] The salts were absorbed into the MOF cavity due to favorable hydrophilic interactions and then reduced to NPs by superhydride (Figures S17–19). This sample exhibited a much lower STY_{MeOH} of 0.58 g_{MeOH} kg_{Cu}^{-1} h^{-1} as compared to that of *in situ* generated NPs in CuZn@UiO-bpy (Table 1; Figure S20), possibly due to less efficient mixing of Cu and Zn. The SPR peak in the diffuse reflectance spectra moved to 590 nm, suggesting larger size of the NPs.

SMSIs from the MOF Support. We hypothesized that both bpydc ligands and Zr_6 SBUs played important roles in the formation of ultrasmall Cu/ZnO_x NPs via SMSIs. To test this hypothesis, we used the double-solvent method to load Cu and Zn into UiO-67 to form DSM-CuZn@UiO-67 (Figure S21). As expected, without bpy moieties to provide SMSI, this catalyst was much less selective for MeOH when compared to DSM-CuZn@UiO-bpy, with a STY_{MeOH} of 0.40 g_{MeOH} kg_{Cu}^{-1} h^{-1} (Table 1). DSM-CuZn@UiO-67 was also not very stable under reaction condition and lost 17% of its initial activity over a 25 h reaction period together with a decrease in MeOH selectivity from 83 to 70% (Figure S22).

To probe the role of Zr_6 SBUs and confinement effects of MOF cavities, we changed the Zr-MOF to an Al-based MOF-253, Al(OH)(bpydc), constructed from $\{Al(OH)(CO_2)\}_n$ chains and bpydc ligands (Figures S23 and S24).[21] The NP/SBU interactions and channel/cavity structures are vastly different between these two MOFs. While UiO-bpy possesses octahedral cages with relatively narrow windows suitable for particle confinement, MOF-253 exhibits rhombic 1D channels 1.2 nm in diameter. Without strong NP/SBU interactions and/or steric hindrance of cavity with small windows in MOF-253, the Cu NPs aggregate to larger nanoparticles 8–10 nm in diameter after the reaction and possibly migrate to the external surface of the MOFs (Figure S25), resulting in an STY_{MeOH} only one-third of that of CuZn@UiO-bpy (Figures S26 and S27). The Cu NPs in this size range also showed strong diffraction peaks in the PXRD patterns (Figure S24).

XPS Studies of Cu/ZnO$_x$ Species and MOF SBUs. The high percentages of Cu/Zn/Zr atoms (>50%) around Cu/ZnO_x and Cu/Zr_6 SBU interfaces in the CuZn@UiO-bpy provide an opportunity to examine the chemical compositions of these interfaces, which constitutes only a low percentage of atoms (<0.1%) in commercial catalysts. We first performed X-ray photoelectron spectroscopy (XPS) studies on Zn@UiO-bpy-Cu (Figure 4a). Before the introduction of reaction gas, Cu existed mostly in the +2 oxidation state (85.4%; Cu $2p_{1/2}$ and $2p_{3/2}$ peaks at 953.4 and 933.6 eV) with only a small amount of

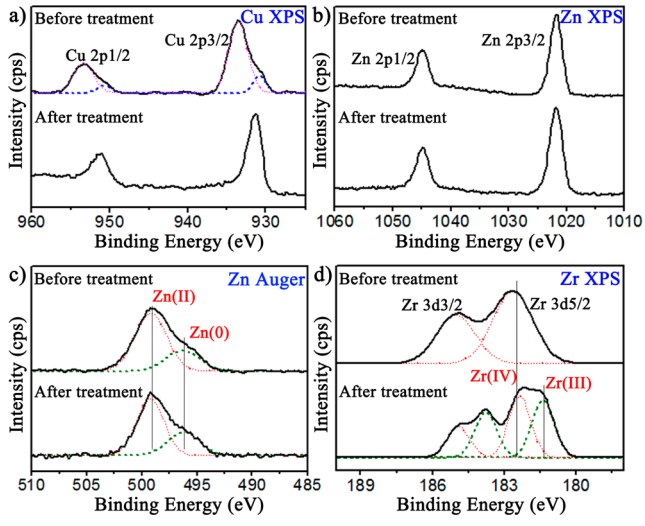

Figure 4. XPS data of Zn@UiO-bpy-Cu before and after introduction of H_2/CO_2 = 3 at 1 atm and 250 °C: (a) Cu 2p region; (b) Zn 2p region; (c) Zn $L_3M_{4.5}M_{4.5}$ Auger peaks; and (d) Zr 3d region.

DOI: 10.1021/jacs.7b00058
J. Am. Chem. Soc. 2017, 139, 3834–3840

Cu(0) species (15%; Cu $2p_{1/2}$ and $2p_{3/2}$ peaks at 950.7 and 930.8 eV). The Cu(0) species likely formed as a result of metathesis recation between (bpydc)$CuCl_2$ and $ZnEt_2$ to form (bpydc)$CuEt_2$, which undergoes reductive elimination to form (bpydc)$Cu(THF)_2$. We detected the formation of butane upon treating UiO-bpy-Cu with $ZnEt_2$ (Figure S28).

Zn@UiO-bpy-Cu was then treated with reaction gas (H_2/CO_2 = 3, 1 bar) at 250 °C in a reaction chamber before transfer again to the XPS chamber through a load−lock gate for analysis without exposure to air. Cu was completely reduced to Cu(0) in the CuZn@UiO-bpy catalyst after treatment (Figure 4a). Notably, Cu was only partially reduced to Cu(0) in Cu@UiO-bpy after the same reduction procedure (Figure S29). When compared to bulk Cu(0) with Cu $2p_{1/2}$ at 952.5 eV, Cu/ZnO_x NPs showed lower Cu binding energy (Cu $2p_{1/2}$ at 951.4 eV), probably as a result of electron injection from the conduction band of ZnO_x to Cu.[22]

The chemical nature of Zn plays an essential role in CO_2 hydrogenation. The Auger Zn $L_3M_{4.5}M_{4.5}$ line serves as a sensitive measurement of the oxidation status of Zn. In XPS spectra of CuZn@UiO-bpy after reacting with the reaction gas flow (1 atm, H_2/CO_2 = 3) at 250 °C, the Zn Auger region consisted of two sets of lines at 498 eV (67%) and 495 eV (33%), attributable to Zn(II) and Zn(0), respectively (Figure 4). In comparison, pure ZnO tablet and Zn@UiO-67, the UiO-67 treated with $ZnEt_2$ but without Cu loading, only showed one line of Zn(II) at 498 eV after treatment with reaction gas (Figure S30), while the commercial tertiary Cu/ZnO/Al_2O_3 catalyst contained only a small amount of Zn(0) (10%) under the same conditions.[23] The presence of Zn(0) species in CuZn@UiO-bpy is either due to rich oxygen vacancies in the ultrasmall ZnO_x NPs or because of Zn alloying into metallic Cu NPs.[24] The Zn(0) Auger peak is more pronounced in the XPS spectra of CuZn@UiO-bpy than those reported in the literature[22] due to a high degree of mixing of Cu and Zn and the formation of ultrasmall NPs. Finally, the XPS data showed a Cu/Zn ratio of 0.86, which is consistent with the ICP-OES results.

The binding energy of Zr band was also measured (Figure 4d). The Zr $3d_{5/2}$ and $3d_{3/2}$ peaks of Zn@UiO-bpy-Cu exhibited binding energies of 182.4 and 184.9 eV respectively, corresponding to the Zr(IV) oxidation state in the $[Zr_6O_4(OH)_4(CO_2)_{12}]$ SBU.[8a,25] After treatment with the reaction gas, the Zr $3d_{5/2}$ band split into two peaks at 182.4 eV (52%) and 181.6 eV (48%), and the Zr $3d_{3/2}$ band split into two peaks at 184.9 eV (41%) and 183.8 eV (59%), suggesting partial reduction of Zr(IV) to Zr(III).[8a] This reduction is likely caused by the spillover of dissociated hydrogen on the Cu surface to the Zr based SBU.

Relationship between Chemisorption of CO_2 and H_2 and Local Structures in Cu/ZnO_x@MOF. *Temperature-Programmed Desorption of H_2.* The presence of Zr and Zn in lower oxidation states has also been supported by temperature-programmed desorption (TPD) profiles of H_2 (Figure 5). The desorption peak of H_2 on metallic Cu sites was not observed because this process takes place at ∼50 °C which was out of the range of our instrument.[26] The temperature in the TPD measurement increased from 100 to 250 °C at a rate of 5 °C/min and then was held at 250 °C for 60 min. The H_2-TPD curve of CuZn@UiO-bpy was deconvoluted into three broad peaks centered at 194, 243, and 250 °C. The first two peaks at 194 and 243 °C were assigned as desorption of hydrogen spilled over onto the Zr-oxide cluster, since they were also present in H_2-TPD of Cu@UiO-bpy but not in that of UiO-bpy. The hydrogen spillover onto zirconia is well-documented in the literature and is responsible for the reduction of Zr(IV) to Zr(III).[27] The third peak in the H_2-TPD of CuZn@UiO-bpy was associated with hydrogen desorption from ZnO_x,[28] as it was also present in the H_2-TPD of CuZn@MOF-253(Al). Furthemore, it was previously shown that Al_2O_3 does not absorb spillover hydrogen.[16]

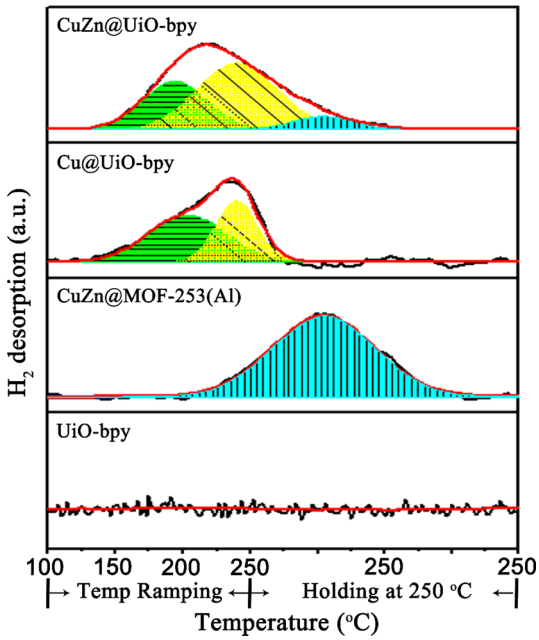

Figure 5. H_2-TPD profiles from 100 to 250 °C. The green and yellow peaks correspond to H_2 desorption on Zr sites, and the cyan peaks are attributed to H_2 desorption on ZnO_x.

TPD of CO_2. Chemisorption of CO_2 on the catalysts was investigated by CO_2-TPD. The temperature was ramped from 100 to 250 °C at a rate of 5 °C/min and then held at 250 °C for 60 min. The CO_2-TPD profile of CuZn@UiO-bpy was deconvoluted into four peaks at 184 and 247 °C, and holding at 250 °C for 3.5 and 12 min (Figure 6). The two strong peaks at >250 °C also appeared in the CO_2-TPD profiles of other UiO-MOF-based samples, even without Cu/Zn metalation, suggesting that they are due to CO_2 adsorption on unsaturated Zr sites on the SBUs. Vacant sites on the Zr-SBUs of UiO MOFs can be generated at relatively low temperatures at 200−250 °C (Figure 7). The 9.1% capping formates on the SBUs can decompose above 200 °C and leave two adjacent 7-coordinated Zr(IV) sites. In fact, even without formate caps, the Zr_6-cluster (SBU) is reported to lose two μ_3-OH and two protons at 250 °C, leaving six 7-coordianted Zr(IV) sites.[14] These open sites can adsorb CO_2 and accept dissociated hydrogen to form Zr−H, likely playing a key role in catalytic CO_2 hydrogenation.

The peak at around 150 °C in the CO_2-TPD profile might be related to bpy site, since it is also present in the profile of UiO-bpy but not in that of UiO-67. The peak around 240 °C can be attributed to Cu NPs since it was also present in the profile of Cu@UiO-bpy. The presence of these multiple sites for CO_2 adsorption was also verified by *in situ* DRIFTS. The multiple negative peaks in the 1400−1750 cm^{-1} region correspond to the carbonate and bicarbonate species absorbed on Cu/ZnO_x or Zr_6 SBU. (Figures S31 and S32).

DOI: 10.1021/jacs.7b00058
J. Am. Chem. Soc. 2017, 139, 3834−3840

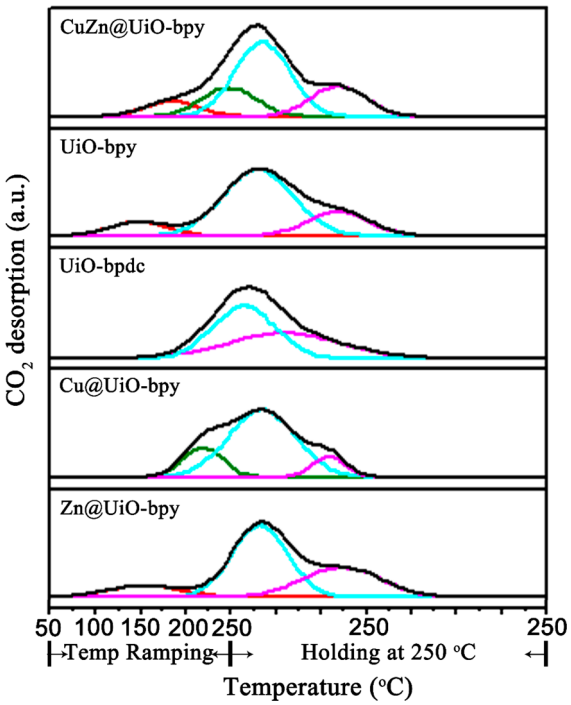

Figure 6. CO_2-TPD profiles of various MOF samples in the 50−250 °C temperature range.

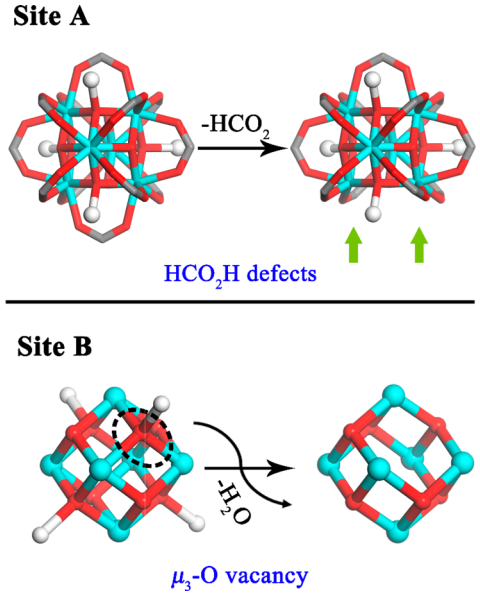

Figure 7. Formation of unsaturated Zr sites that can accept CO_2 and hydrogen spillovered from Cu surfaces.

DISCUSSION

Our experimental findings indicate that rich surface/interface sites on well-mixed Cu, ZnO_x, and Zr_6 SBUs contribute to the adsorption and activation of H_2 and CO_2 in the CuZn@UiO-bpy catalyst (Figure 8). Based on established mechanistic understanding of the $Cu/ZnO/Al_2O_3$ catalyst, we propose that H_2 first undergoes homolytic dissociation on the Cu surface to form Cu−H species. The dissociated hydrogen spillovers to Zr sites on the SBUs and defect sites on ZnO_x. Meanwhile, CO_2 is adsorbed on unsaturated Zr sites and ZnO_x to form carbonates and bicarbonates, which are quickly hydrogenated by the activated hydrogen from spillover. The spillover hydrogen can also reduce some Zr(IV) to Zr(III) and some Zn(II) to Zn(0), as observed by XPS. The synergystic combination of hydrogen activation sites on Cu and CO_2 activation sites on ZnO_x and Zr SBUs leads to superior performance of the CuZn@UiO-bpy catalyst.

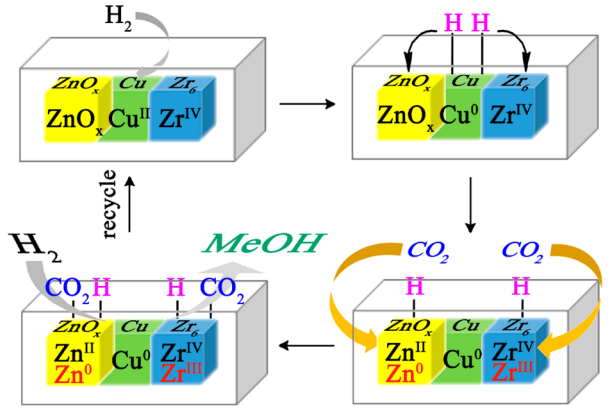

Figure 8. Schematic showing the encapsulated active sites in MOFs and the functions of the various surface sites in catalytic CO_2 hydrogenation.

CONCLUSION

We have generated ultrasmall Cu/ZnO_x nanoparticles in MOF cavities *in situ* under CO_2 hydrogenation conditions. The strong interactions between Cu/ZnO_x nanoparticles and the bpy moieties on the ligands as well as Zr_6 SBUs stabilize these ultrasmall well-mixed nanoparticles and prevent the agglomeration of Cu NPs and phase separation between Cu and ZnO_x. A high degree of mixing between Cu and ZnO_x leads to formation of low-valence Zn and Zr in the presence of H_2 at 250 °C, affording high catalytic activity and selectivity for methanol synthesis from CO_2 hydrogenation. Our work highlights new opportunities in using MOFs as novel supports for metal nanoparticle catalysts by taking advantage of tunable and specific strong metal−support interactions.

ASSOCIATED CONTENT

Supporting Information

The Supporting Information is available free of charge on the ACS Publications website at DOI: 10.1021/jacs.7b00058.

General experimental; procedures for catalyst characterization; catalyst preparation and evaluation of catalytic performance, including additional catalytic data and TEM images of catalysts before and after reactions; XPS analysis; and *in situ* DRIFT spectra (PDF)

AUTHOR INFORMATION

Corresponding Authors

*wangchengxmu@xmu.edu.cn
*wenbinlin@uchicago.edu

ORCID

Cheng Wang: 0000-0002-7906-8061
Wenbin Lin: 0000-0001-7035-7759

Notes

The authors declare no competing financial interest.

DOI: 10.1021/jacs.7b00058
J. Am. Chem. Soc. 2017, 139, 3834−3840

■ ACKNOWLEDGMENTS

We thank Zi Wang and Ruihan Dai for experimental help. We acknowledge funding support from the National Natural Science Foundation and Ministry of Science and Technology of the P. R. of China (NSFC21471126, NSFC21671162, and 2016YFA0200702), the National Thousand Talents Program of the P. R. of China, the 985 Program of Chemistry and Chemical Engineering Disciplines of Xiamen University, and the U.S. National Science Foundation (DMR-1308229)

■ REFERENCES

(1) (a) Olah, G. A.; Goeppert, A.; Prakash, G. K. S. *Beyond Oil and Gas: The Methanol Economy*; Wiley-VCH: Weinheim, 2009. (b) Porosoff, M. D.; Yan, B.; Chen, J. G. *Energy Environ. Sci.* **2016**, *9*, 62−73.

(2) (a) Razali, N. A. M.; Lee, K. T.; Bhatia, S.; Mohamed, A. R. *Renewable Sustainable Energy Rev.* **2012**, *16*, 4951−4964. (b) Wang, W.; Wang, S.; Ma, X.; Gong, J. *Chem. Soc. Rev.* **2011**, *40*, 3703−3727. (c) Chen, X.; Li, C.; Graetzel, M.; Kostecki, R.; Mao, S. S. *Chem. Soc. Rev.* **2012**, *41*, 7909−7937.

(3) (a) Lee, S. Methanol synthesis from syngas. In *Handbook of Alternative Fuel Technologies*; Lee, S., Speight, J. G., Loyalka, S. K., Eds.; CRC Press LLC: Boca Raton, FL, 2007; pp 297−321. (b) Kunkes, E. L.; Studt, F.; Abild-Pedersen, F.; Schloegl, R.; Behrens, M. *J. Catal.* **2015**, *328*, 43−48.

(4) Wilmer, H.; Genger, T.; Hinrichsen, O. *J. Catal.* **2003**, *215*, 188−198.

(5) (a) van den Berg, R.; Prieto, G.; Korpershoek, G.; van der Wal, L. I.; van Bunningen, A. J.; Laegsgaard-Joergensen, S.; de Jongh, P. E.; de Jong, K. P. *Nat. Commun.* **2016**, *7*, 13057. (b) Behrens, M.; Studt, F.; Kasatkin, I.; Kuehl, S.; Haevecker, M.; Abild-Pedersen, F.; Zander, S.; Girgsdies, F.; Kurr, P.; Kniep, B.-L.; Tovar, M.; Fischer, R. W.; Norskov, J. K.; Schloegl, R. *Science* **2012**, *336*, 893−897. (c) Meunier, F. C. *Angew. Chem., Int. Ed.* **2011**, *50*, 4053−4054. (d) Didziulis, S. V.; Butcher, K. D.; Cohen, S. L.; Solomon, E. I. *J. Am. Chem. Soc.* **1989**, *111*, 7110−23.

(6) Fichtl, M. B.; Schlereth, D.; Jacobsen, N.; Kasatkin, I.; Schumann, J.; Behrens, M.; Schlögl, R.; Hinrichsen, O. *Appl. Catal., A* **2015**, *502*, 262−270.

(7) (a) Kanai, Y.; Watanabe, T.; Fujitani, T.; Saito, M.; Nakamura, J.; Uchijima, T. *Catal. Lett.* **1994**, *27*, 67−78. (b) Stone, F. S.; Waller, D. *Top. Catal.* **2003**, *22*, 305−318.

(8) (a) Rungtaweevoranit, B.; Baek, J.; Araujo, J. R.; Archanjo, B. S.; Choi, K. M.; Yaghi, O. M.; Somorjai, G. A. *Nano Lett.* **2016**, *16*, 7645−7649. (b) Kattel, S.; Yan, B.; Yang, Y.; Chen, J. G.; Liu, P. *J. Am. Chem. Soc.* **2016**, *138*, 12440. (c) Weigel, J.; Koeppel, R. A.; Baiker, A.; Wokaun, A. *Langmuir* **1996**, *12*, 5319−5329. (d) Bonura, G.; Cordaro, M.; Spadaro, L.; Cannilla, C.; Arena, F.; Frusteri, F. *Appl. Catal., B* **2013**, *140*−*141*, 16−24. (e) Lunkenbein, T.; Schumann, J.; Behrens, M.; Schlogl, R.; Willinger, M. G. *Angew. Chem., Int. Ed.* **2015**, *54*, 4544−8. (f) Muller, M.; Hermes, S.; Kaehler, K.; van den Berg, M. W. E.; Muhler, M.; Fischer, R. A. *Chem. Mater.* **2008**, *20*, 4576−4587. (g) Arena, F.; Mezzatesta, G.; Zafarana, G.; Trunfio, G.; Frusteri, F.; Spadaro, L. *J. Catal.* **2013**, *300*, 141−151. (h) Gascon, J.; Aguado, S.; Kapteijn, F. *Microporous Mesoporous Mater.* **2008**, *113*, 132−138.

(9) Behrens, M.; Zander, S.; Kurr, P.; Jacobsen, N.; Senker, J.; Koch, G.; Ressler, T.; Fischer, R. W.; Schloegl, R. *J. Am. Chem. Soc.* **2013**, *135*, 6061−6068.

(10) (a) Wang, J.; Lu, S.-m.; Li, J.; Li, C. *Chem. Commun.* **2015**, *51*, 17615−17618. (b) Zhong, M.; Zhang, X.; Zhao, Y.; Li, C.; Yang, Q. *Green Chem.* **2015**, *17*, 1702−1709.

(11) (a) Pan, L.; Liu, H.; Lei, X.; Huang, X.; Olson, D. H.; Turro, N. J.; Li, J. *Angew. Chem., Int. Ed.* **2003**, *42*, 542−546. (b) Zhao, M.; Yuan, K.; Wang, Y.; Li, G.; Guo, J.; Gu, L.; Hu, W.; Zhao, H.; Tang, Z. *Nature* **2016**, *539*, 76−80. (c) Lu, G.; Li, S.; Guo, Z.; Farha, O. K.; Hauser, B. G.; Qi, X.; Wang, Y.; Wang, X.; Han, S.; Liu, X.; DuChene, J. S.; Zhang, H.; Zhang, Q.; Chen, X.; Ma, J.; Loo, S. C.; Wei, W. D.; Yang, Y.; Hupp, J. T.; Huo, F. *Nat. Chem.* **2012**, *4*, 310−6. (d) Wang, C.; deKrafft, K. E.; Lin, W. *J. Am. Chem. Soc.* **2012**, *134*, 7211−7214. (e) Cai, G.; Jiang, H. L. *Angew. Chem., Int. Ed.* **2017**, *56*, 563−567. (f) Santos, V. P.; Wezendonk, T. A.; Nasalevich, M. A.; Sartipi, S.; Sun, X.; Hakeem, A. A.; Kapteijn, F.; Makkee, M.; Gascon, J.; Jaen, J. J. D.; Dugulan, A. I.; Islam, H.-U.; Sankar, G.; Chojecki, A.; Koeken, A. C. J.; Ruitenbeek, M.; Davidian, T.; Meima, G. R. *Nat. Commun.* **2015**, *6*, 6451.

(12) (a) Choi, K. M.; Na, K.; Somorjai, G. A.; Yaghi, O. M. *J. Am. Chem. Soc.* **2015**, *137*, 7810−7816. (b) Zhang, T.; Manna, K.; Lin, W. *J. Am. Chem. Soc.* **2016**, *138*, 3241−3249. (c) Yan, J. M.; Wang, Z. L.; Gu, L.; Li, S. J.; Wang, H. L.; Zheng, W. T.; Jiang, Q. *Adv. Energy Mater.* **2015**, *5*, 1500107.

(13) (a) Manna, K.; Ji, P.; Lin, Z.; Greene, F. X.; Urban, A.; Thacker, N. C.; Lin, W. *Nat. Commun.* **2016**, *7*, 12610. (b) Manna, K.; Ji, P.; Greene, F. X.; Lin, W. *J. Am. Chem. Soc.* **2016**, *138*, 7488−7491. (c) Yang, D.; Odoh, S. O.; Wang, T. C.; Farha, O. K.; Hupp, J. T.; Cramer, C. J.; Gagliardi, L.; Gates, B. C. *J. Am. Chem. Soc.* **2015**, *137*, 7391−7396. (d) Nguyen, H. G. T.; Schweitzer, N. M.; Chang, C. Y.; Drake, T. L.; So, M. C.; Stair, P. C.; Farha, O. K.; Hupp, J. T.; Nguyen, S. T. *ACS Catal.* **2014**, *4*, 2496−2500. (e) Yang, D.; Odoh, S. O.; Borycz, J.; Wang, T. C.; Farha, O. K.; Hupp, J. T.; Cramer, C. J.; Gagliardi, L.; Gates, B. C. *ACS Catal.* **2016**, *6*, 235−247. (f) Li, Z.; Peters, A. W.; Bernales, V.; Ortuño, M. A.; Schweitzer, N. M.; DeStefano, M. R.; Gallington, L. C.; Platero-Prats, A. E.; Chapman, K. W.; Cramer, C. J.; Gagliardi, L.; Hupp, J. T.; Farha, O. K. *ACS Cent. Sci.* **2017**, *3*, 31−38.

(14) Wu, H.; Chua, Y. S.; Krungleviciute, V.; Tyagi, M.; Chen, P.; Yildirim, T.; Zhou, W. *J. Am. Chem. Soc.* **2013**, *135*, 10525−10532.

(15) Toyao, T.; Miyahara, K.; Fujiwaki, M.; Kim, T. H.; Dohshi, S.; Horiuchi, Y.; Matsuoka, M. *J. Phys. Chem. C* **2015**, *119*, 8131−8137.

(16) Gao, P.; Li, F.; Zhan, H.; Zhao, N.; Xiao, F.; Wei, W.; Zhong, L.; Wang, H.; Sun, Y. *J. Catal.* **2013**, *298*, 51−60.

(17) (a) Brown, N. J.; García-Trenco, A.; Weiner, J.; White, E. R.; Allinson, M.; Chen, Y.; Wells, P. P.; Gibson, E. K.; Hellgardt, K.; Shaffer, M. S. P.; Williams, C. K. *ACS Catal.* **2015**, *5*, 2895−2902. (b) Curtis, A. C.; Duff, D. G.; Edwards, P. P.; Jefferson, D. A.; Johnson, B. F. G.; Kirkland, A. I.; Wallace, A. S. *J. Phys. Chem.* **1988**, *92*, 2270−2275.

(18) Bonura, G.; Cordaro, M.; Cannilla, C.; Arena, F.; Frusteri, F. *Appl. Catal., B* **2014**, *152*−*153*, 152−161.

(19) Creighton, J. A.; Eadon, D. G. *J. Chem. Soc., Faraday Trans.* **1991**, *87*, 3881−3891.

(20) Chen, Y. Z.; Zhou, Y. X.; Wang, H.; Lu, J.; Uchida, T.; Xu, Q.; Yu, S.-H.; Jiang, H. L. *ACS Catal.* **2015**, *5*, 2062−2069.

(21) Bloch, E. D.; Britt, D.; Lee, C.; Doonan, C. J.; Uribe-Romo, F. J.; Furukawa, H.; Long, J. R.; Yaghi, O. M. *J. Am. Chem. Soc.* **2010**, *132*, 14382−14384.

(22) Liao, F.; Huang, Y.; Ge, J.; Zheng, W.; Tedsree, K.; Collier, P.; Hong, X.; Tsang, S. C. *Angew. Chem., Int. Ed.* **2011**, *50*, 2162−2165.

(23) (a) Kuld, S.; Conradsen, C.; Moses, P. G.; Chorkendorff, I.; Sehested, J. *Angew. Chem., Int. Ed.* **2014**, *53*, 5941−5945. (b) Aksela, S.; Väyrynen, J.; Aksela, H. *Phys. Rev. Lett.* **1974**, *33*, 999−1002.

(24) (a) Ullah Awan, S.; Hasanain, S. K.; Bertino, M. F.; Hassnain Jaffari, G. *J. Appl. Phys.* **2012**, *112*, 103924. (b) Schott, V.; Oberhofer, H.; Birkner, A.; Xu, M.; Wang, Y.; Muhler, M.; Reuter, K.; Wöll, C. *Angew. Chem., Int. Ed.* **2013**, *52*, 11925−11929.

(25) Long, J.; Wang, S.; Ding, Z.; Wang, S.; Zhou, Y.; Huang, L.; Wang, X. *Chem. Commun.* **2012**, *48*, 11656−11658.

(26) Muhler, M.; Nielsen, L. P.; Törnqvist, E.; Clausen, B. S.; Topsøe, H. *Catal. Lett.* **1992**, *14*, 241−249.

(27) (a) Kouva, S.; Honkala, K.; Lefferts, L.; Kanervo, J. *Catal. Sci. Technol.* **2015**, *5*, 3473−3490. (b) Syzgantseva, O. A.; Calatayud, M.; Minot, C. *J. Phys. Chem. C* **2012**, *116*, 6636−6644.

(28) Larmier, K.; Liao, W.-C.; Tada, S.; Lam, E.; Verel, R.; Bansode, A.; Urakawa, A.; Comas-Vives, A.; Copéret, C. *Angew. Chem., Int. Ed.* **2017**, *56*, 2318.

DOI: 10.1021/jacs.7b00058
J. Am. Chem. Soc. 2017, 139, 3834−3840